Journal of Nuclear Materials 376 (2008) 229–239

Contents lists available at ScienceDirect

Journal of Nuclear Materials

journal homepage: www.elsevier.com/locate/jnucmat

A comparison of Stefan and Phase Field modeling techniques for the simulation of melting nuclear fuel

M.J. Welland, B.J. Lewis *, W.T. Thompson

Department of Chemistry and Chemical Engineering, Royal Military College of Canada, P.O. 17000 Station Forces, Kingston, Ontario, Canada K7K 7B4

ARTICLE INFO

Article history:
Received 4 December 2007
Accepted 5 March 2008

ABSTRACT

Simulations of heat transfer in UO_2 at very high temperatures incorporating the effects of phase transitions are being conducted to help support the design and analysis of experimental work being conducted as part of nuclear safety research. This work includes the interpretation of the behaviour of nuclear fuel under conditions where centerline melting may occur. Models based on the Stefan formulation and Phase Field approach are derived from fundamental principles and implemented using recently published material properties. Both simulations compare well with laser flash experiments in recently published literature. The Phase Field model is recommended for further development due to its versatility in handling heat sources and robustness in simulating the evolution of the solid–liquid interface. These points are demonstrated with an example simulation of centerline melting resultant from fission heating for fuel performance analysis.

1. Introduction

Under upset or very high power conditions, it is possible that local fuel melting may result. A number of mechanistic codes have been developed for reactor safety analysis to predict the thermal mechanical behaviour of nuclear fuel elements under upset or severe reactor accident conditions, where fuel melting phenomena can occur [1–5]. In addition, even under normal operating conditions, fuel centerline melting may result with defective fuel operation at high linear power ratings, where the thermal performance of the element may be degraded with the possibility of fuel oxidation, which leads to a reduced thermal conductivity in the urania and a lower incipient melting temperature in the hyperstoichiometric fuel [6–8].

Recent experiments have been performed to better understand molten fuel phenomena, typically involving laser flash techniques [9] or a furnace as performed by Latta and Fryxell [10], i.e. specialized equipment is required to heat fuel samples to the melting temperature of 3147 K for unoxidized fuel. These experiments therefore provide a methodology to study the thermal properties of uranium dioxide fuel and hyperstoichiometric fuel at high temperature in both the solid and liquid state. In order to determine such properties, sophisticated models coupling the heat and mass transport are typically needed [11]. There is also a requirement to generalize these models so that they can be used in fuel performance and safety codes. For example, in these latter applications, a non-idealized geometry may be present where there is not just surface heating but rather a volumetric source of heat due to decay, fission or chemical processes in fuel elements under various operating conditions and accident scenarios. The introduction of a phase transformation adds significant complexity to the fuel behaviour models due to sharply changing material properties. In particular, as a simplification to incorporate such phenomena, the thermal effects of a phase change have been previously modeled by considering rapid changes in the enthalpy or heat capacity over a given temperature interval [12]. A more fundamental treatment, however, is desirable in order to assess such approximate approaches for treating molten fuel behaviour, which is the focus of the current modelling effort.

In working towards simulating the melting of an operational fuel element, two modelling techniques are developed. The Stefan formulation is essentially the law of conservation of energy as it applies to a moving phase boundary. This approach is widely used for modelling problems with changing phases [13,14] and has previously been applied by Atrazhev and Brykin [11] to describe the melting of nuclear fuel by laser flash experiments. The Phase Field technique is commonly used to simulate solidification microstructure [15] but offers many attributes desirable to simulations of melting on the scale of interest in this work. In contrast with the Stefan formulation, the Phase Field model does not solve for the position and rate of movement of the phase change front but rather can deduce it from the solution. Boettinger et al. [16] presents an excellent review of this methodology but derives an isothermal formulation to which a heat flow equation is appended. Bi and Sekerka [17] derive a general formulation for the non-isothermal case

* Corresponding author. Tel.: +1 613 541 6000x6611; fax: +1 613 542 9489.
E-mail address: lewis-b@rmc.ca (B.J. Lewis).

0022-3115/$ - see front matter Crown Copyright © 2008 Published by Elsevier B.V. All rights reserved.
doi:10.1016/j.jnucmat.2008.03.003

which forms the basis of the derivation presented herein. To our knowledge, the Phase Field model has not been applied to the problem of nuclear fuel melting.

This work therefore details the theoretical development of both models and assesses their suitability for nuclear fuel analysis. The models are specifically compared to results from laser flash experiments that were previously conducted at the Institute for Transuranium elements (ITU). The application of the Phase Field model to fuel centerline melting in an operating fuel element is also demonstrated.

2. Modelling techniques

The development of the Stefan and Phase Field models to describe heat and mass transfer in liquid and solid uranium dioxide fuel is described in Sections 2.1 and 2.2, respectively.

2.1. The Stefan formulation

The Stefan formulation is based on the conservation of energy in the presence of a moving melting/solidifying front which is explicitly tracked. Local equilibrium is assumed on either side of this boundary and undercooling/superheating effects are ignored. This conception is considered a 'sharp interface' model since the phase change is assumed to be localized to a stable, well defined melting front without a two phase 'mushy region'.

The basic schematic of the Stefan formulation, defining the normal direction $\hat{n}$ in accordance with the convention in [18], is shown in Fig. 1. All symbols are listed for reference in the nomenclature section in Table 1.

The heat transport equation for the temperature T must be satisfied in both the liquid and solid phases independently:

$$\rho \cdot C_p \frac{\partial T}{\partial t} = -\vec{\nabla} \cdot \vec{q} + \dot{Q} \tag{1}$$

where ρ is the density, C_p is the heat capacity, $\dot{Q}$ is volumetric heat generation and $\vec{q}$ is the fourier heat flux defined as

$$\vec{q} = -k\vec{\nabla}T \tag{2}$$

in which k is the thermal conductivity.

The temperature profile in the sample is continuous across the boundary and equal to the melting temperature. The heat flux is discontinuous across the moving phase change front as a consequence of the storage of enthalpy of fusion. Indicating solid and liquid fluxes by the subscripts S and L, the conservation equation may be written as

$$\vec{q}_{\mathrm{L}} \cdot \hat{n} - \vec{q}_{\mathrm{S}} \cdot \hat{n} = \rho \Delta H_{\mathrm{fus}} R_{\mathrm{fus}} \tag{3}$$

where R_{fus} is the rate of fusion, and ΔH_{fus} is the enthalpy of fusion.

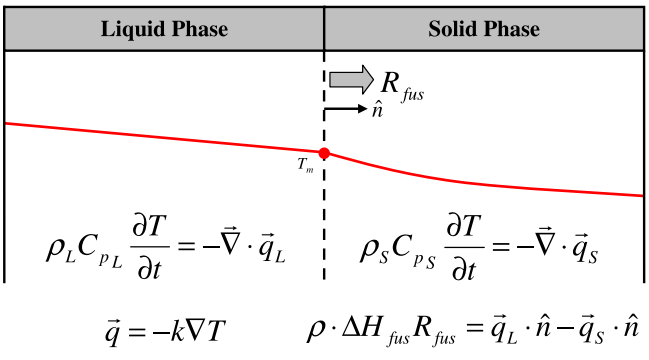

Fig. 1. Stefan model schematic with liquid and solid phases separated by a sharp interface. This figure defines the normal vector and the rate of fusion R_{fus}.

Table 1
Nomenclature

Symbol	Definition
a	Radius of a fuel pellet
A	Area
C_{eff}	Reduced fraction of effusion rate due to buffer gas pressure
C_p	Heat capacity
d	Height of sapphire window above sample surface
f	Helmholtz energy density
f_θ	Heterogeneous nucleation factor
g	Gibbs energy density
h	Enthalpy density
I^o	Kinetic parameter for nucleation
$I_{0,1}$	Modified Bessel functions
k	Thermal conductivity
k_{B}	Boltzmann's constant
k_{He}	Thermal conductivity of helium
K_u	Excess energy of interface
K_s	Excess entropy of interface
M	Molar mass of vapour species
M_u	Mobility of internal energy
M_φ	Kinetic parameter of phase change
n	Number of atoms
$\hat{n}$	Normal direction
p	Smoothing function
P_{lin}	Linear power
P_{max}	Maximum power incident on the sample
P_{pulse}	Observed laser pulse shape
P_{vap}	Vapour pressure above UO_2
$\vec{q}$	Fourier heat flux
q_{c}	Conductive heat flux
q_{laser}	Incident laser power on sample
q_{r}	Radiative heat flux
q_{v}	Vapourization heat flux
$\dot{Q}$	Volumetric heat source
s	Entropy density
S	Entropy
R_{fus}	Rate of fusion
t	Time
T	Temperature
T_m	Melting temperature
T_∞	Ambient temperature
u	Internal energy density
V	Volume
W	Height of potential barrier in $K_u(\varphi)$
$\vec{x}$	Spatial coordinates
$\vec{X}$	Reference coordinates
δ	Interface thickness parameter
Δg_{fus}	Gibbs energy of fusion per unit volume
ΔG_{fus}	Gibbs energy of fusion
ΔG_{n}	Gibbs energy of nucleus formation
$\Delta G_{\mathrm{n}}^{\mathrm{o}}$	Critical energy for nucleus formation
ΔH_{fus}	Enthalpy of fusion
ΔH_{vap}	Enthalpy of vapourization
ε	Emissivity
ε_φ	Coefficient of gradient in φ
κ	Inverse neutron diffusion length
ρ	Density
σ	Surface energy between solid and liquid
σ_{SB}	Stefan Boltzmann constant
φ	Phase field variable
$\dot{\varphi}_{\mathrm{n}}$	Rate of phase change due to nucleation
$\vec{\Psi}$	Velocity of the mesh with respect to the material
$'$	Derivative with respect to φ
$\bullet$	Derivative with respect to time

It is important to note that the rate of the phase front movement is independent of any motion of the liquid phase. The rate of front movement is the rate of melting for positive values and conversely the rate of solidification for negative values. The Stefan problem is then described completely by Eqs. (1)–(3).

The moving phase front is represented mathematically as a boundary between the solid and liquid phase that moves with time. One technique to model a moving boundary problem is to perform a coordinate transformation from the moving 'spatial' do-

main (such as would be observed) to a stationary 'reference' domain upon which the equations may be solved. Such a transformation may be accomplished via the Arbitrary Lagrange Eulerian method [19] which introduces a new set of unknown variables, i.e., $\vec{x}$ which correspond to the observed, spatial coordinate system. These variables, in addition to the unknowns of the problem, are solved on the stationary, reference domain with coordinates $\vec{X}$. The solution, $\vec{x}(\vec{X})$ allows for the transformation of the problem unknowns and their derivatives between the reference and spatial domains as illustrated in Fig. 2. Using temperature as an example, the transformation of spatial and temporal derivatives are

$$\nabla_{\vec{x}} T = \nabla_{\vec{X}} T \cdot \frac{\partial \vec{X}}{\partial \vec{x}} \tag{4}$$

$$\frac{DT}{Dt} = \frac{\partial T}{\partial t} + \nabla_{\vec{x}} T \cdot \vec{\Psi} \tag{5}$$

where subscripts denote the coordinate system for the given derivative, $\frac{D}{Dt}$ represents the total (material) time derivative and $\vec{\Psi} = \frac{\partial \vec{X}}{\partial t}$ is the velocity of the mesh with respect to the material. The temporal derivative includes a convective term to account for the mesh movement. The term $\frac{\partial \vec{X}}{\partial \vec{x}}$ in Eq. (4) is the inverse Jacobian of this transformation. In the one dimensional case, this term takes the simple form:

$$\frac{\partial \vec{x}}{\partial \vec{X}} = \frac{\partial x}{\partial X} \tag{6}$$

$$\frac{\partial \vec{X}}{\partial \vec{x}} = \frac{\partial x^{-1}}{\partial X} \tag{7}$$

Mesh displacement or velocity is determined for all points on the reference mesh by the solution of a smoothing equation such as $\nabla^2_{\vec{X}} \vec{\Psi} = 0$ subject to the boundary conditions. In the current model, outer boundaries are stationary and the internal boundary is fixed to the melting front so that the mesh follows the movement of the interface.

2.2. Phase Field model

The Phase Field model adds a scalar variable φ, named the phase field variable, to the problem domain and an associated partial differential equation to govern it [20]. This variable is an abstract parameterization of the extent to which a region of material may be considered solid or liquid. It can be interpreted as the local fractional volume that is liquid, or proportional to the regularity of atomic spacing [21]. It is not a conserved quantity. In this development, φ represents the phase change between solid and liquid for clarity, but it can represent any phase transformation in general.

In this analysis, the value of φ varies continuously in the range [0,1] representing solid and liquid, respectively. For $\varphi \neq 0, 1$, a two phase region is present in which the material can be considered a mix of solid and liquid forming a 'diffuse' interface in contrast to the sharp interface used in other models such as the Stefan formulation previously described [22]. This formulation is a very general model which can be shown to reduce to the Stefan condition in the sharp interface limit.

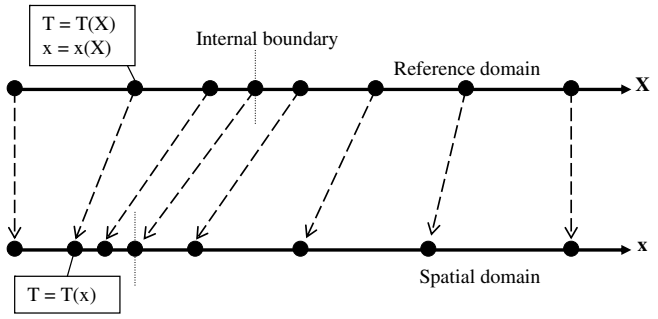

Fig. 2. An example coordinate transformation between the reference and spatial domains in one dimension. The temperature $T(X)$ and the transformed coordinates $x(X)$ are computed on the reference domain. They are combined in order to reproduce the temperature on the moving, spatial domain: $T(X) = T(x(X)^{-1})$.

The theory of irreversible processes is employed to derive the equations governing φ and its relation to classical heat flux. This theory is founded on the Laws of Thermodynamics [23], particularly the Second Law: in an isolated process, the local entropy production is positive [24]. As derived in the Appendix, the Phase Field model requires the solution of the following set of partial differential equations for the temperature T in the generalized heat conduction equation and the phase change φ, respectively:

$$\rho C_p \frac{\partial T}{\partial t} = \vec{\nabla} \cdot k \vec{\nabla} T - [p'(\varphi) \Delta H_{\text{fus}}(T) + K'_u(\varphi)] \cdot \frac{\partial \varphi}{\partial t} + \dot{Q} \tag{8}$$

$$\frac{\partial \varphi}{\partial t} = -M_\varphi \left(\frac{1}{T} [p'(\varphi) \cdot \Delta G_{\text{fus}}(T) + K'_u(\varphi)] - \varepsilon^2_\varphi \vec{\nabla}^2 \varphi \right) + \dot{\varphi}_{\text{n}} \tag{9}$$

Here $(')$ denotes differentiation with respect to φ. The thermodynamic functions ΔH_{fus} and ΔG_{fus} are the enthalpy and Gibbs energy of fusion, respectively, which are also used in phase equilibrium packages such as CALPHAD or FACT. The term M_φ is a kinetic parameter for the rate of phase change and ε_φ is the coefficient of the gradient term in the entropy functional as described in the Appendix. Material properties are expressed according to a linear progression in φ between solid and liquid values as shown below for k using subscripts S and L to denote the solid and liquid states, respectively:

$$k(T, \varphi) = (1 - p(\varphi)) \cdot k_{\text{S}}(T) + p(\varphi) \cdot k_{\text{L}}(T) \tag{10}$$

The function $p(\varphi)$ smoothes φ and allows the enforcement of certain requirements as outlined in the Appendix. The function $K_u(\varphi)$ describes the excess surface energy of the material on the boundary between solid and liquid where $\varphi \neq 0, 1$. As in other work, these parameters are taken to be [16]:

$$p(\varphi) = \varphi^3 [6\varphi^2 - 15\varphi + 10] \tag{11}$$

$$K_u(\varphi) = W \varphi^2 [1 - \varphi]^2 \tag{12}$$

where W is the height of the energy peak.

Additional Phase Field constants are given by

$$W = 6\sigma/\delta \tag{13}$$

$$\varepsilon^2_\varphi = 12\sigma\delta/T_{\text{m}} \tag{14}$$

$$M_\varphi = \frac{k}{5} \left(\frac{T_{\text{m}}}{\delta \cdot \Delta H_{\text{fus}}} \right)^2 \tag{15}$$

where σ is the surface energy between solid and liquid phases, δ is a user-chosen measure of the interface thickness and T_{m} is the melting temperature.

The term $\dot{\varphi}_{\text{n}}$ in Eq. (9) describes nucleation of one phase inside another and is given by

$$\dot{\varphi}_{\text{n}} = \exp\left(-\frac{\Delta G^o_n}{k_{\text{B}} T} \right) \cdot \begin{cases} I^o_{\text{S}}(1 - \varphi) & \text{if} \quad \Delta G_{\text{fus}} < 0 \\ -I^o_{\text{L}} \varphi & \text{if} \quad \Delta G_{\text{fus}} > 0 \end{cases} \tag{16}$$

where ΔG^o_n is the critical energy for a nucleus, k_{B} is Boltzmann's constant and the constants $I^o_{\text{S,L}}$ are related to nucleation kinetics.

The width of the diffuse interface can be envisioned as a balance between the opposing energy effects described by W and ε_φ. The former increases the energy of material on the boundary, which tends to make the interface sharp. The later increases the energy associated a rapid change in φ, which tends to make the interface more diffuse [16]. Hence, these two parameters provide a means to control the spatial extent of the interface region which has implications with computational resources as discussed below.

The Phase Field model does not explicitly define the position of the interface, but rather includes it indirectly. This technique allows for complex interface shapes, volumetric heating and undercooling/superheating effects that can pose difficulties in other simulation techniques. Herein lies the power of the Phase Field methodology.

3. Model implementation and validation

The current model is being benchmarked against experiments conducted at the Institute for Transuranium Elements (ITU) in Karlsruhe, Germany, in which measurements of the melting transition in UO_2 are obtained [9,25]. This experimental work is used to verify the development of the modelling techniques in this analysis.

Briefly, in the ITU experiment, a prepared sample of UO_2 is held in a high pressure helium buffer gas to suppress the extent of UO_3 vapourization. The sample is heated on one side with a combination of two lasers whose beams are homogenized by random mixing over a long fiber optic cable. One laser is used at lower power to slow and condition the cooling rate to prevent undercooling which would complicate the modelling procedure. The other laser is used at higher intensity to heat the surface of the sample and induce melting. A sapphire window was placed 1 mm above the sample to reduce convective currents. The surface temperature in the center of the pellet is then recorded using optical pyrometers.

The proposed models require the solution of a set of highly nonlinear differential equations which were solved using the commercial finite element software platform, Comsol Multiphysics version 3.3. Since the experiment provided a measurement of the surface temperature at the center of the molten pool, this quantity is the variable of interest for model validation.

Energy is assumed to be deposited uniformly on the surface of the sample in accordance with the observed pulse profile, $P_{\text{pulse}}(t)$, where the maximum power, $P_{\max}$, is set empirically from the simulation results. In accordance with Kirchhoff's radiation law [26], the absorptivity is taken to be equal to the emissivity, ε, yielding the formula for incident energy flux, q_{laser}:

$$q_{\text{laser}} = \varepsilon \cdot P_{\max} P_{\text{pulse}}(t) \tag{17}$$

Heat is lost from the surface of the sample through conduction into the buffer gas (q_c) and radiative heat transfer (q_r) as given by the flux expressions:

$$q_c = \frac{k_{\text{He}}}{d}(T - T_\infty) \tag{18}$$

$$q_r = \varepsilon\sigma_{\text{SB}}(T^4 - T_\infty^4) \tag{19}$$

where k_{He} is the thermal conductivity of Helium [27], d is the height of the sapphire window, T_∞ is the ambient temperature and σ_{SB} is the Stefan Boltzmann's constant.

The high pressure buffer gas is assumed to suppress mass vapourization of UO_3 to inhibit a stoichiometry change in the sample. Thus vapourization is only included as a heat loss, q_v, where a Knudsen effusion formula is applied to account for this loss [28]:

$$q_v = \Delta H_{\text{vap}} \cdot C_{\text{eff}} \cdot \left(\frac{44.3}{\sqrt{M}} \cdot \frac{P_{\text{vap}}}{\sqrt{T}}\right) \tag{20}$$

where ΔH_{vap} is the molar enthalpy of vapourization, $P_{\text{vap}}(T)$ is the vapour pressure [29] and M is the molar mass of the vapour species. In order to correct for the buffer gas pressure, this formula includes a constant fraction C_{eff}, which is selected to reproduce the observed temperature profile. This approximation has been shown to be sufficiently accurate in other work [12]. The melting temperature is set to the value reported in the experiment: 3156 K.

Material properties for this simulation are given in Table 2 and are primarily taken from the Fink review in 2000 [30]. Although a more recent review by Ronchi [31] is available, thermal properties from the Fink review are chosen for consistency. The melting temperature is inputted as 3156 K in order to coincide with the experimental observations. The interface width δ in Eqs. (13)–(15) is

Table 2
Input material properties

Property	Equation	Units
Solid		
C_p	$52.1743 + 87.951T_k - 84.2411T_k^2 + 31.542T_k^3 - 2.6334T_k^4 - .71391T_k^{-2}$	J/mol K
k	$\frac{100}{7.5408+17.692T_k+3.614T_k^2} + 6400T_k^{-5/2}\exp\left(\frac{-16.35}{T_k}\right)$	W/m K
P_{vap}	$10^{-31284/T + 7.616}$[29]	MPa
ΔH_{vap}	514 000[a]	J/mol
ε	$0.836 + 4.321 \cdot 10^{-6}(T - 3120)$	
ρ	10.5[b]	g/cm^3
Liquid		
C_p	$0.25136 + 1328.8T_k^{-2}$	J/mol K
k	3.1[c]	W/m K
P_{vap}	$10^{(15.961-26974/T)}T^{-2.76}$	MPa
ε	$1 - 0.16096 \cdot \exp(-3.7897 \cdot 10^{-4}(T - 3120) - 3.2718 \cdot 10^{-7}(T - 3120)^2)$	
ΔH_{vap}	$516382 - 22.946T$	J/mol
ρ	10.5	g/cm^3
General properties		
k_{He}	$0.152\left(\frac{T}{300}\right)^{0.71}$[27]	W/m K
T_m	3156[9]	K
ΔG_{fus}	$-26496 + 621.3T - 84.58T\ln(T) + 0.0440T^2 - 1.404 \cdot 10^{-5}T^3 + 2.629 \cdot 10^{-9}T^4 - 1.317 \cdot 10^{-13}T^5 - 356955/T$ [6][d]	J/mol
ΔH_{fus}	70 000	J/mol
σ	0.06[e]	J/m^2

Material properties for $\varphi \neq 0, 1$ are linear interpolations between solid and liquid values. For simplification, $T_k = T/1000$ and are both in *K*. Material properties are from Ref. [30] unless otherwise noted.

[a] Calculated as the sum of the enthalpy of vapourization at the specified melting temperature and the enthalpy of fusion and assumed to be constant.
[b] 95% theoretical density. As volume expansion is not simulated, no temperature dependence is implemented.
[c] The choice of this value is discussed in Sections 5.
[d] This expression is modified from Ref. [6] in order to set the melting point at 3156 K.
[e] The surface energy between a liquid and solid phase is assume to be the difference in the free surface energies of each stated in [30].

limited by the computational resources and set to 0.1 μm and 10 μm for the one and two dimensional Phase Field model, respectively. The nucleation rate constants, I_L^o and I_S^o in Eq. (16) are chosen to prevent undercooling/superheating for this experiment.

4. Results

Fig. 3 shows the results of three simulations in comparison to the experimental work. A one dimensional simulation with the Stefan model assuming axial symmetry is compared to the Phase Field model in one and two dimensions. As depicted in the figure, the plot can be divided into four stages, where:

1. The sample is completely solid and being heated rapidly by the combined laser pulses.
2. The surface temperature has passed the melting temperature. There are now two phases present; a liquid phase near the surface of the sample, and the bulk solid phase. The liquid phase grows with time until a maximum temperature is reached. After this point, the heating laser is turned off and the sample cools rapidly until the free surface temperature reaches the melting temperature again. Concurrently, the liquid region is resolidifying against the underlying solid.
3. The free surface liquid temperature reaches the melting (freezing) temperature and starts to solidify. Solidification now advances from both the surface and the bulk into the liquid. As the liquid solidifies, the latent heat is released, forming a temperature plateau until all of the liquid is resolidified.
4. The liquid phase is now completely solidified and only one phase remains. The temperature slowly becomes uniform over the sample. A slight kink appears in the temperature profile when the conditioning laser is turned off.

The Phase Field simulations are shown for a time of 57 ms where the one dimensional model (taken along the axis of the sample) is shown in Fig. 4, and the two dimensional model (assuming azimuthally symmetry) is show in Fig. 5 which shows the radial extent of the molten pool.

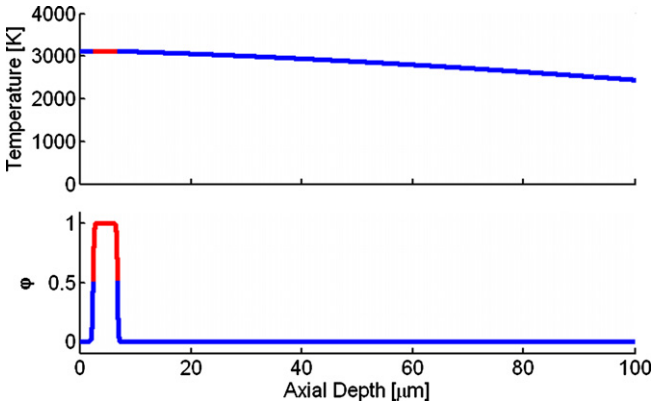

Fig. 4. One dimensional Phase Field model showing temperature and φ for $t = 57$ ms.

5. Sensitivity analysis

The sensitivity of the models to the thermophysical material properties was investigated with the Stefan formulation, which is particularly sensitive to the rate of energy deposition on the surface. This result is partially affected by the ablation of the material being heated, which removes heat as the enthalpy of vapourization (in addition to an attenuation of the laser beam intensity above the sample surface).

Decreasing the interface thickness δ, and so approaching the sharp interface limit, did not yield an appreciable effect in the one dimensional simulation. Increasing the value of the nucleation constants $I_{S,L}^o$ above the value at which undercooling/superheating was not observed also did not affect the results appreciably, but did cause some instability in the convergence of the solution.

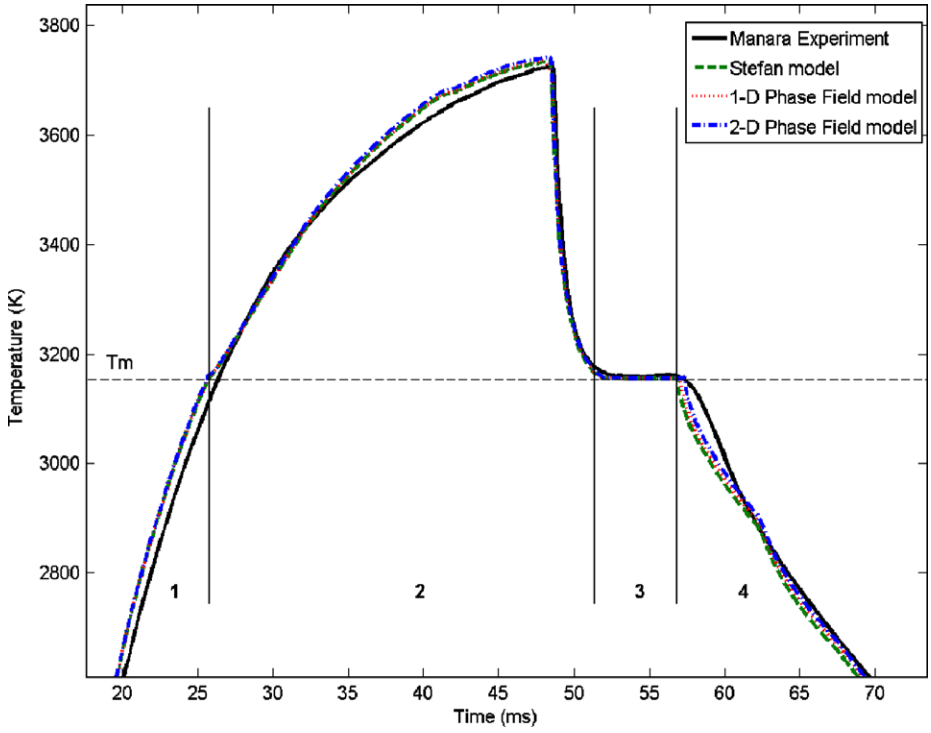

Fig. 3. Comparison of the Stefan formulation model, the one and two dimensional Phase Field models and the experimental observation. The melting point for the models is set to coincide with the results of the experiment for the purpose of comparison.

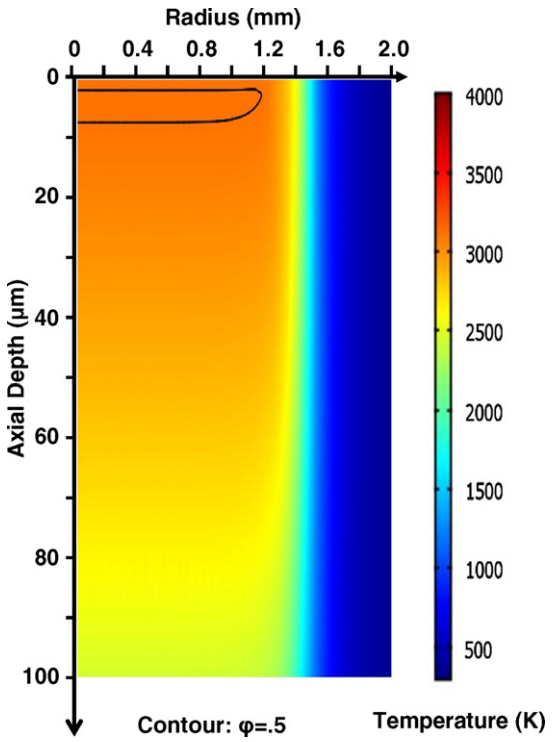

Fig. 5. Two dimensional Phase Field model showing enclosed molten material for $t = 57$ ms.

The current model does not include volume change due to thermal expansion. Therefore the density was chosen to be a constant in both phases in order to conserve mass. The choice of the initial density reported in [25] was 10.5 g/cm^3 (95% of the theoretical density). The simulation result using this value was compared against the solid and liquid densities at the melting point, 9.1 g/cm^3 and 8.4 g/cm^3, respectively, calculated using the thermal expansion equation from [30], where no noticeable effect was observed. The effect of thermal expansion will be considered in future work.

The thermal conductivity of the liquid has a large uncertainty. Fink recommends a value of 2.5 ± 1 W/m K whereas Sheindlin et al. [12] recommends a value of 2.6 ± .35 W/m K. The effect of this uncertainty is shown in Fig. 6, which shows that the main effect is on the duration of the temperature plateau (which increases with a an increasing thermal conductivity value). This result can be conceptually explained where more energy is reaching the solid through the liquid, for the same apparent surface temperature. The results presented in Fig. 3 employ a value of 3.1 W/m K that provides the best simulation of the observed thermogram within the reported uncertainty. The inclusion of thermal expansion may help further reconcile this value with that reported in the literature.

6. Discussion

For the application of these models to the problem of fuel melting in operating fuel elements, a comparison of the abilities of the Stefan and Phase Field models needs to be considered in terms of the ease and stability of computational implementations and the capability to include the relevant physical phenomena such as fission heating.

Numerically solving the system of differential equations requires the definition of a mesh on the domain of interest. The resolution of this mesh is a major factor in determining the required computational resources. In order to obtain accurate results, it is important that the mesh be well resolved in regions of large physical property variations. For the melting/freezing case, the region around the interface contains sharp gradients and discontinuities in the physical properties. As the presented Stefan formulation explicitly determines the position and speed of the interface, the moving mesh can maintain high resolution mesh regions around

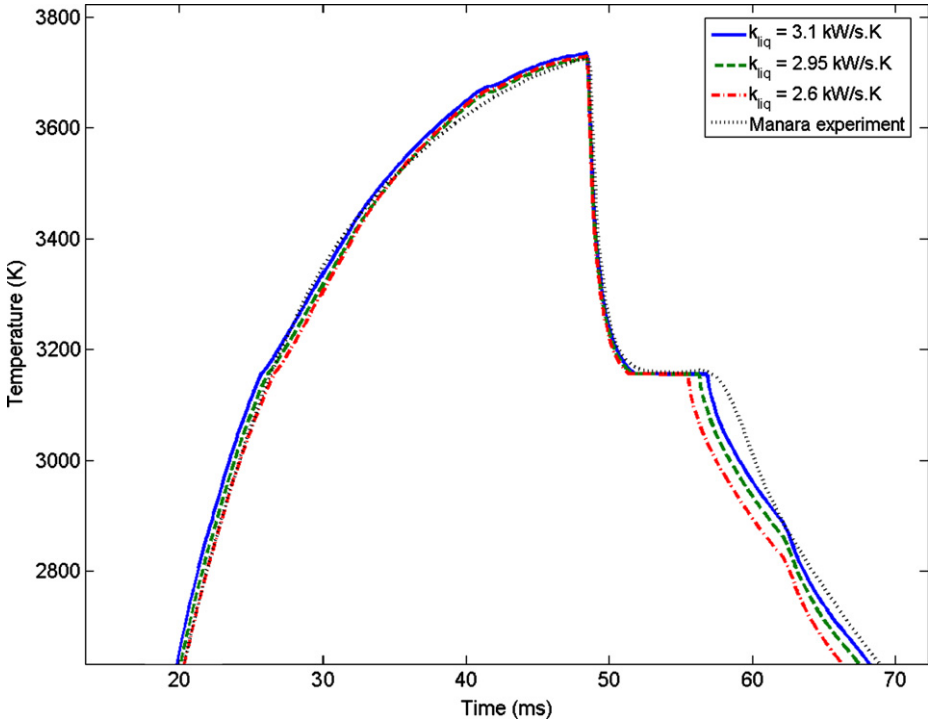

Fig. 6. Comparison of the effects of different thermal conductivities in the liquid phase.

the front. This implementation reduces the overall computational requirements by allowing a coarser mesh to be used for the bulk of the material while keeping fine resolution in the region of interest. In contrast, since the Phase Field approach does not explicitly track the boundary, the mesh must be adequately resolved over the entire domain where the interface could be found. As discussed in the Appendix, this requirement implies that the mesh resolution should be approximately one order of magnitude less than the specified interface width. This substantially increases the computational requirements of this model and makes it impractical for large and especially multi-dimensional domains.

While the material properties in the Phase Field model vary smoothly and continuously from solid to liquid, the Stefan formulation requires individually defined regions for solid and liquid phases. This requirement is accomplished in this work by solving the model in a series of stages in accordance to those outlined in Fig. 3. Changing between stages presents a challenge and introduces instability into the overall model. Knowledge is also required *a priori* of the sequence of stages, or a more sophisticated code.

Unfortunately, the Stefan model cannot easily accommodate volumetric heating, as occurs by fission in operational fuel elements. This limitation is due to the assumption of a stable, sharp interface, and the derivation of the rate of interface movement described in Eq. (3). In this formulation, the movement of the interface may only occur as a result of heat flow across the interface. This restriction has implications in the situation of fission heating in which heat is generated throughout the volume of the material. In this case, heat is no longer required to cross the boundary and will therefore not advance the melting front despite potentially raising the temperature above the melting point. Since the Phase Field method does not solve for interface movement explicitly, it does not suffer from this limitation.

The potential for the Phase Field model to accommodate volumetric heating is further demonstrated in this work by considering a volumetric source term for nuclear fission heating in an unirradiated, naturally-enriched cylindrical nuclear fuel element (of radius a = 6.075 mm), where:

$$\dot{Q}(r) = \frac{P_{\text{lin}}}{\pi a^2}\left[\frac{\kappa a}{2I_1(\kappa a)}\right] I_0(\kappa r) \tag{21}$$

This expression accounts for neutron flux depression effects in the element in the radial direction r, where P_{lin} is the linear power, $\kappa = 0.9\ \text{cm}^{-1}$ is the inverse neutron diffusion length and $I_{0,1}$ are the modified Bessel functions. A constant fuel pellet surface temperature of 700 K is assumed as a Dirchlet boundary condition at $r = a$. For the simulation, the pellet is assumed to start from a uniform temperature equal to the surface temperature. Fig. 7 shows the results of this simulation for a series of linear powers. This analysis shows that centerline melting is first expected at approximately 84 kW/m. For this simulation, no change in the model implementation is required beyond a change in the boundary conditions, the addition of a volumetric heat source and a conversion to cylindrical coordinates. Since the material properties and governing differential equations are unchanged in this analysis, this result demonstrates the versatility of the Phase Field model for use in experimental design and analysis (i.e., to deduce material properties) and for application in safety and fuel performance analysis.

The Phase Field approach easily includes nucleation and undercooling neither of which has been included in the Stefan formulation. While not important for modeling this experiment, this may become important in volumetric heating and cases where constitutional undercooling may be introduced as a consequence of treating

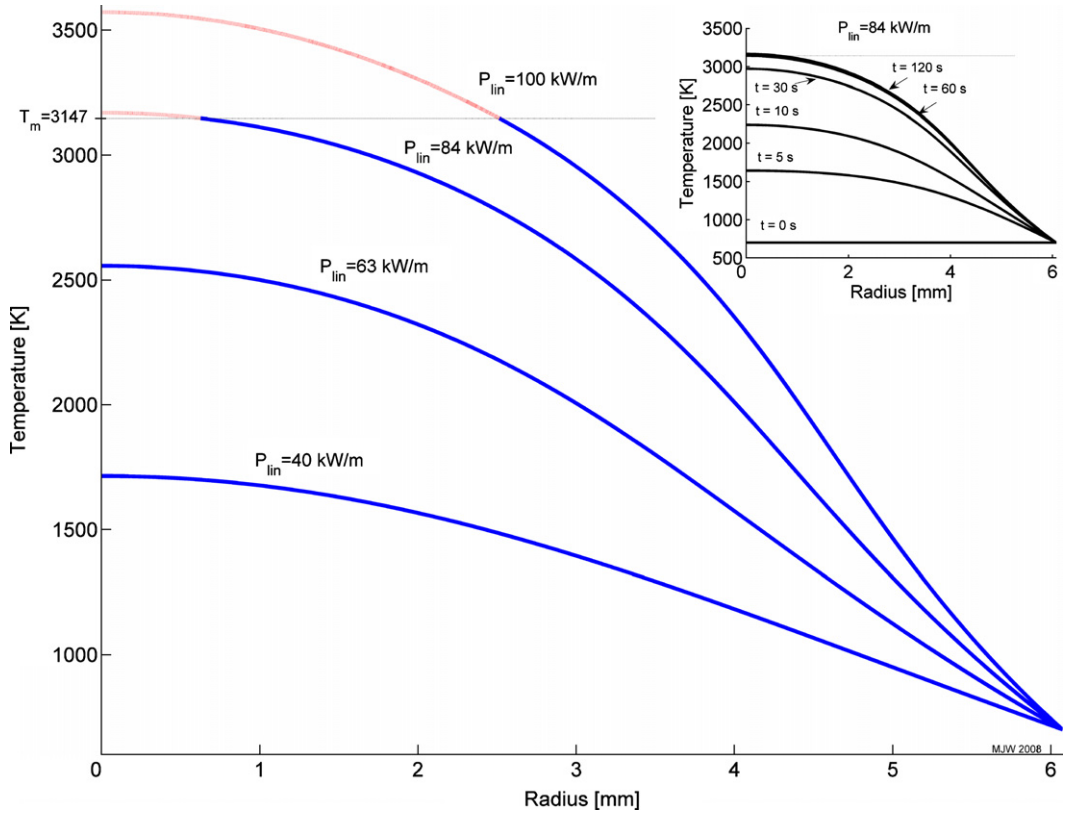

Fig. 7. Example simulation of an unirradiated, naturally-enriched CANDU fuel element operating at various linear powers. Inset shows the progression of the temperature profile for P_{lin} = 84 kW/m.

non-stoichiometric fuel, UO_{2+x}, where the melt hyperstoichiometry exceeds that of the solid at the interface.

7. Conclusions

The current results demonstrate that both the Stefan and Phase Field concepts are sound and mutually consistent with the experimental laser flash results. The agreement between the one and two dimensional Phase Field model indicates that a one dimensional analysis is sufficiently accurate. Both the Stefan formulation and the Phase Field model have been shown to be capable of simulating non-congruent phase transitions in other work [16,22]. However as previously discussed and demonstrated, the Phase Field model is better suited to describe centerline melting phenomenon in operating fuel elements with a volumetric (fission) heat source in nuclear fuel.

The Phase Field model has been selected for the advancement of this work to include non-stoichiometric UO_{2+x} that can occur if the fuel elements was to become defected during operation. The case of UO_{2+x} is complicated by the change in melting temperature with stoichiometry as well as varying material properties. However the success of the current work, and particularly the robustness of the Phase Field model, suggest that this model may be a more appropriate and general tool for such analysis.

Acknowledgements

This work was funded by a Defence Research and Development Board [DRDB] scholarship and a Collaborative Research and Development grant from the Natural Sciences and Engineering Research Council of Canada [NSERC]. We wish to thank Dr Manara for his advice and discussions of experiments at ITU. We would also like to acknowledge the late Dr Faramarz Akbari for his contributions to this work both in subject material and in support through friendship.

Appendix. Phase Field derivation

The physical quantities and governing equations of the Phase Field model are derived and evaluated in this appendix.

Derivation of the general equation

To determine the total entropy S in a volume V, a general entropy functional is proposed in the form [32,33]

$$S = \int_V \left(s(u,\varphi) - \frac{\varepsilon_\varphi^2}{2} |\vec{\nabla}\varphi|^2 \right) \mathrm{d}V \tag{22}$$

where $s(u,\varphi)$ is the local entropy density given as a function of the internal energy density u and the Phase Field variable φ. The constant ε_φ characterizes the energy effect of a gradient in φ. Using dot notation to indicate time derivatives, the rate of change of the entropy may be derived:

$$\frac{\mathrm{d}S}{\mathrm{d}t} = \int_V \left(\frac{\partial s}{\partial u}\dot{u} + \frac{\partial s}{\partial \varphi}\dot{\varphi} - \varepsilon_\varphi^2 \vec{\nabla}\varphi \vec{\nabla}\dot{\varphi} \right) \mathrm{d}V \tag{23}$$

The First Law of thermodynamics is applied via

$$\dot{u} = -\vec{\nabla}\cdot\vec{q} + \dot{Q} \tag{24}$$

where $\vec{q}$ is the heat flux and $\dot{Q}$ is a volumetric heat source such as fission. This equation can be substituted into Eq. (23) and rearranged through Green's Theorem and the Divergence Theorem to yield:

$$\underbrace{\frac{\mathrm{d}S}{\mathrm{d}t}}_{\text{Entropy change}} = \underbrace{\int_V \left(\vec{\nabla}\frac{\partial s}{\partial u}\cdot\vec{q} + \left[\frac{\partial s}{\partial \varphi} + \varepsilon_\varphi^2 \vec{\nabla}^2\varphi \right] \dot{\varphi} \right) \mathrm{d}V}_{\text{Entropy produced by irreversible processes}} - \underbrace{\int_A \left(\frac{\partial s}{\partial u}\cdot\vec{q} + \varepsilon_\varphi^2 \dot{\varphi}\vec{\nabla}\varphi \right)\cdot\hat{n}\,\mathrm{d}A}_{\text{Flux across boundary}} + \underbrace{\int_V \left(\frac{\partial s}{\partial u}\cdot\dot{Q} \right) \mathrm{d}V}_{\text{Volumetric generation}} \tag{25}$$

where A is the boundary of V and the last term accounts for entropy introduced into the system that is not a result of a flux across the boundary or an internal irreversible process.

As the entropy produced in a system is always positive for a real system and since Eq. (25) is valid for an arbitrary volume then:

$$\vec{\nabla}\frac{\partial s}{\partial u}\cdot\vec{q} + \left[\frac{\partial s}{\partial \varphi} + \varepsilon_\varphi^2 \vec{\nabla}^2\varphi \right] \dot{\varphi} > 0 \tag{26}$$

This inequality may be ensured by assuming:

$$\vec{q} = M_u \cdot \vec{\nabla}\frac{\partial s}{\partial u} \tag{27}$$

$$\dot{\varphi} = M_\varphi \left(\frac{\partial s}{\partial \varphi} + \varepsilon_\varphi^2 \vec{\nabla}^2\varphi \right) \tag{28}$$

where M_u and M_φ are always positive and couple the driving forces to the resulting fluxes [17]. The mobility of the internal energy, M_u, is phenomenological and will be shown to be related to the well-known Fourier heat flux. The term M_φ is related to attachment kinetics and determines the rate of phase change.

The solution of the Phase Field model requires a solution of Eqs. (24) and (28) subject to the flux expression in Eq. (27). These two equations are coupled by the expression of the entropy density function $s(u,\varphi)$.

State functions

The general energy and entropy density equations for a pure material may be written respectively as

$$u(T,\varphi) = [1 - p(\varphi)]u_S(T) + p(\varphi)u_L(T) + K_u(\varphi) \tag{29}$$

$$s(T,\varphi) = [1 - p(\varphi)]s_S(T) + p(\varphi)s_L(T) + K_s(\varphi) \tag{30}$$

where $p(\varphi)$ is an interpolation function of the phase parameter such that $p(\varphi = 0) = 0$ and $p(\varphi = 1) = 1$. The functions $K_u(\varphi)$ and $K_s(\varphi)$ describe the effects of a mixture of two phases in the form of surface energy and entropy of mixing for a solution of solid and liquid phases. Assuming that the number of separate phase regions (such as solid nuclei in a liquid phase) is not large, $K_s(\varphi) \cong 0$. The form of $K_u(\varphi)$ is arbitrary; it does not change the sharp interface limit and will be discussed further below.

Thermodynamic driving forces

The internal energy flux given in Eq. (27) may now be expanded by noting the definition of thermodynamic temperature [34], leading to the recovery of the Fourier conductive heat flux:

$$\frac{\partial s}{\partial u} = \frac{1}{T} \tag{31}$$

$$\vec{q} = M_u \cdot \vec{\nabla}\frac{1}{T} = -\frac{M_u}{T^2}\vec{\nabla}T = -k\cdot\vec{\nabla}T \tag{32}$$

where the thermal conductivity has been introduced as $k = M_u/T^2$. The rate of change of internal energy is assumed to be approximately equal to the rate of change of the enthalpy, $\dot{h}$, due to the small thermal expansion of condensed phases. Using $(')$ to denote differentiation with respect to φ:

$$\dot{h}(T,\varphi) \cong \dot{u}(T,\varphi) = \rho C_p \dot{T} + \left[p'(\varphi)\Delta H_{\mathrm{fus}} + K_u'(\varphi) \right] \cdot \dot{\varphi} + \dot{Q} \tag{33}$$

The generalized heat conduction, Eq. (8) may be derived:

$$\begin{aligned}\dot{u} &= -\vec{\nabla}\cdot\vec{q} + \dot{Q} \\ \rho C_p \dot{T} &= \vec{\nabla}\cdot k\vec{\nabla}T - [p'(\varphi)\Delta H_{\text{fus}} + K'_u(\varphi)]\cdot\dot{\varphi} + \dot{Q}\end{aligned} \tag{34}$$

where ΔH_{fus} is the enthalpy of fusion.

In expanding Eq. (28), the $\frac{\partial s(u,\varphi)}{\partial\varphi}$ term requires the notion of the total derivative [35] in order to make use of Eqs. (29) and (30).

$$\begin{aligned}\frac{\partial s(u,\varphi)}{\partial\varphi} &= \frac{Ds(u,\varphi)}{D\varphi} - \frac{\partial s}{\partial u}\frac{\partial u(T,\varphi)}{\partial\varphi} \\ &= \frac{\partial s(T,\varphi)}{\partial\varphi} - \frac{1}{T}\frac{\partial u(T,\varphi)}{\partial\varphi} \\ &= p'(s_{\text{L}} - s_{\text{S}}) - \frac{1}{T}[p'\cdot(u_{\text{L}} - u_{\text{S}}) + K'_u] \\ &= -\frac{1}{T}[p'\cdot(f_{\text{L}} - f_{\text{S}}) + K'_u]\end{aligned} \tag{35}$$

where $f = u - Ts$ is the Helmholtz energy density. Using Eq. (35) and assuming the approximate equality between internal energy and enthalpy again, $\Delta G_{\text{fus}}(T) \cong f_{\text{L}}(T) - f_{\text{S}}(T)$, Eq. (28) becomes:

$$\dot{\varphi} = -M_\varphi\left(\frac{1}{T}[p'(\varphi)\cdot\Delta G_{\text{fus}}(T) + K'_u(\varphi)] - \varepsilon_\varphi^2\vec{\nabla}^2\varphi\right) \tag{36}$$

where ΔG_{fus} is the Gibbs energy of fusion and ε_φ is the coefficient of the gradient term.

Nucleation

The onset of crystallization within a liquid requires a critical number of atoms to surmount a potential barrier and assemble in a specific configuration as a result of random thermofluctuations [36]. Nucleation may more properly be simulated in compliance with statistical mechanics by Langevin-noise terms [37]; however, due to the relatively large scale of this application, elementary nucleation theory is instead inserted *ad hoc* into Eq. (36).

The Gibbs energy ΔG_n associated with the formation of a spherical embryo of n atoms, in the solid configuration, is comprised of the bulk and boundary energies:

$$\Delta G_n = V\Delta g_{\text{fus}} + A\sigma \tag{37}$$

where A is the area bounding a volume V, σ is the surface energy and Δg_{fus} is the Gibbs energy change per unit volume [38]. The volumetric term (proportional to the cube of the embryo radius) is negative below the melting point and increases in magnitude monotonically whereas the surface energy (proportional to the square of the embryo radius) is always positive. For a small embryo, the surface energy increase will outweigh the volumetric decrease, preventing the embryo's growth. As depicted in Fig. 8, there is a maximum in ΔG_n at which point the addition of molecules will reduce the total energy of the cluster and the embryo will begin to grow.

The maximum, ΔG_n^o for a spherical cluster is given as [39]:

$$\Delta G_n^o = \frac{16\pi}{3}\left(\frac{\sigma^3}{\Delta g^2}\right)f_\theta \tag{38}$$

where f_θ is the heterogeneous nucleation factor which depends on the wetting angle. This factor accounts for the reduction in nucleation activation energy by impurities, defects or foreign solids and greatly reduces the degree of undercooling during solidification.

Assuming an equilibrium concentration of clusters and basic growth kinetics, an Arrhenius type expression (with activation energy ΔG_n^o) for the nucleation rate may be derived:

$$I = I^o\exp\left(-\frac{\Delta G_n^o}{k_{\text{B}}T}\right) \tag{39}$$

where I^o is related to attachment kinetics and k_{B} is Boltzmann's constant.

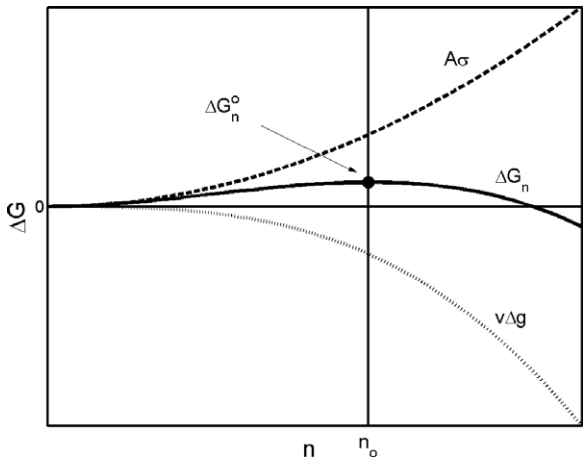

Fig. 8. Embryo Gibbs energy as a function of the number of atoms in an embryo, showing the critical value ΔG_n^o.

The onset of liquid growth is assumed to behave in much the same way, except that the kinetics are much faster due removal of the restriction that atoms have to be placed at specific lattice sites. Thus initial solid and liquid growth is incorporated into the Phase Field model by the addition of a source term into Eq. (36) of the form given in Eq. (16).

Determination of Phase Field constants

The choice of the interpolation function $p(\varphi)$ and the excess interfacial energy $K_u(\varphi)$ are now investigated. The function $p(\varphi)$ necessarily has properties that $p(\varphi = 0) = 0$ and $p(\varphi = 1) = 1$. The function $K_u(\varphi)$ has the form of a double well potential having minima at $\varphi = 0, 1$ and a maximum at $\varphi = 0.5$. The height of this potential barrier is proportional to a constant W which will be shown to relate to the surface energy later.

The Gibbs energy expression may be derived from Eqs. (29) and (30):

$$G(T,\varphi) = G_S(T) + p(\varphi)\cdot\Delta G_{\text{fus}}(T) + K_u(\varphi) \tag{40}$$

At the melting temperature $G_{\text{S}} = G_{\text{L}}$. Furthermore, in order to make the solid and liquid phase stable, $G(T,\varphi)$ must have local equilibriums at $\varphi = 0, 1$ for all temperatures. Applied to Eq. (40) these constraints impart the following assertions on $K_u(\varphi)$ and $p(\varphi)$ [40]:

$$\begin{aligned}&K_u(0) = K_u(1) = 0 \\ &[K'_u(\varphi) + p'(\varphi)\cdot\Delta G_{\text{fus}}]_{\varphi=0,1} = 0 \\ &[K''_u(\varphi) + p''(\varphi)\cdot\Delta G_{\text{fus}}]_{\varphi=0,1} > 0\end{aligned} \tag{41}$$

Within the confines of these constraints, the actual form of these equations is arbitrary; the choice does not affect the sharp interface limit. For this implementation, a common choice [16] is employed as plotted in Figs. 9 and 10.

$$p(\varphi) = \varphi^3[6\varphi^2 - 15\varphi + 10] \tag{42}$$

$$K_u(\varphi) = W\varphi^2[1-\varphi]^2 \tag{43}$$

It is now possible to use the sharp interface model to determine the constants W, ε_φ and M_φ and infer their meaning and physical relevance. To proceed, consider the case of an equilibrium solution in one dimension (planar interface) at the melting temperature T_m. The heat balance equation is satisfied and Eq. (9) becomes:

$$\begin{aligned}0 &= -M_\varphi\left(\frac{1}{T_m}[p'(\varphi)\cdot\Delta G_{\text{fus}}(T_m) + K'_u(\varphi)] - \varepsilon_\varphi^2\vec{\nabla}^2\varphi\right) \\ \varepsilon_\varphi^2\vec{\nabla}^2\varphi &= \frac{2W}{T_m}[\varphi(\varphi-1)(2\varphi-1)]\end{aligned} \tag{44}$$

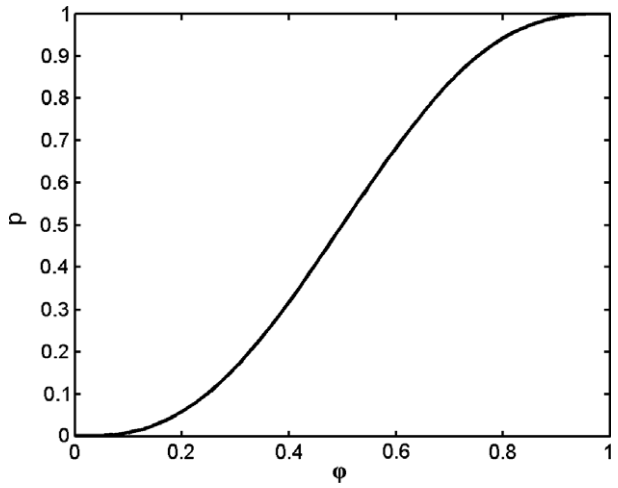

Fig. 9. The interpolation function $p(\varphi)$.

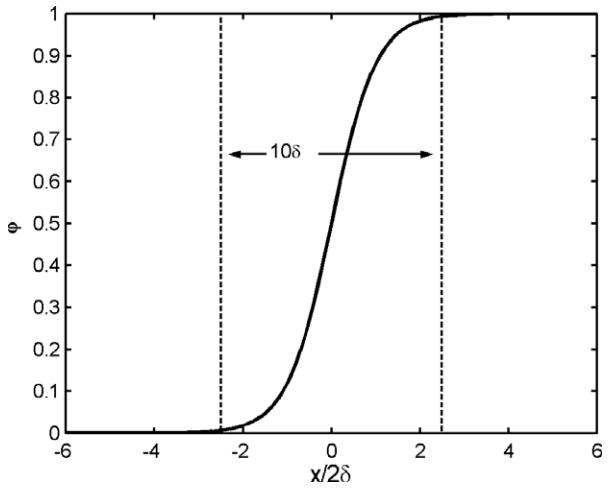

Fig. 11. Steady state solution for φ. The input parameter δ determines the width of the resulting interface.

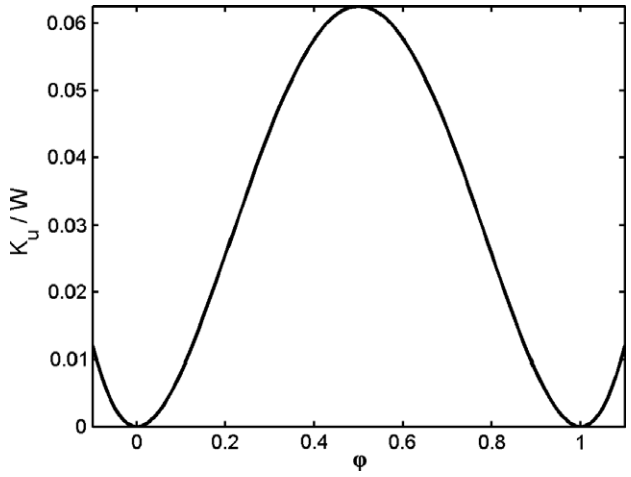

Fig. 10. The double well potential function $K_u(\varphi)$.

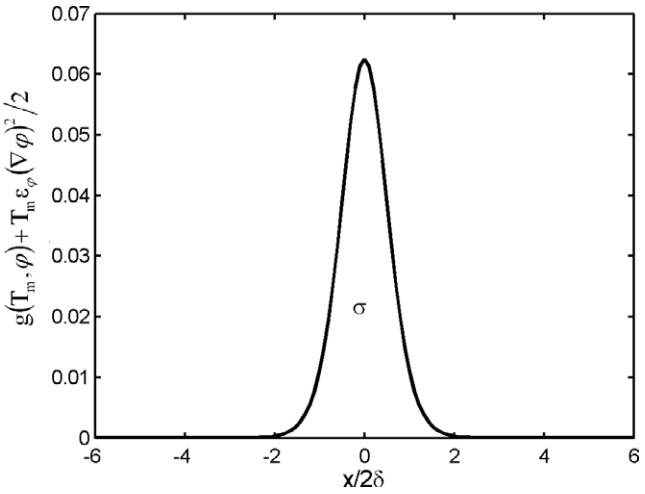

Fig. 12. Excess energy of material in the interface for the steady state solution.

for which a solution exists:

$$\varphi(x) = \frac{1}{2}\left[1 + \tanh\left(\frac{x}{2\delta}\right)\right] \tag{45}$$

where

$$\delta = \varepsilon_\varphi \sqrt{\frac{T_m}{2W}} \tag{46}$$

The constant δ can be interpreted as a measure of interface thickness as is shown graphically in Fig. 11. This is a useful parameter to control since the mesh size for the computational domain must be of comparable size in order to adequately resolve the interface.

Assuming that the internal energy functional does not have any gradient components and using Eq. (22), the Gibbs energy functional may be written as:

$$G = \int_V \left(g(T,\varphi) + T\frac{\varepsilon_\varphi^2}{2}|\vec{\nabla}\varphi|^2 \right) \mathrm{d}V \tag{47}$$

where g is the Gibbs energy density as a function of temperature and phase.

The excess energy term associated with the boundary, the surface energy, is given by the gradient term above. A plot of this energy over the steady state solution in Eq. (45) is shown in Fig. 12.

This can also be integrated to obtain an expression for the surface energy:

$$\sigma = \frac{\varepsilon_\varphi}{6}\sqrt{\frac{WT_\mathrm{m}}{2}} \tag{48}$$

Eqs. 46 and 48 can be rearranged to determine expressions for W and ε_φ as presented in Eqs. (13) and (14).

The mobility of φ, corresponding to the rate of phase growth, is related to the interface kinetics. The relationship between the accuracy of the solution and the interface width δ has been studied and an expression for M_φ that is accurate to second order in δ was derived for the case of equal thermal conductivities in the solid and liquid phase at the melting point, and a small interface thickness [41]. Since the thermal conductivities for the two phases are close in value, the assumption of a constant thermal conductivity in the model is reasonable:

$$\frac{1}{M_\varphi} = \frac{6\delta\Delta H_\mathrm{fus}}{T_\mathrm{m}^2}\left[\frac{1}{\mu} + A\left(\frac{\delta\cdot\Delta H_\mathrm{fus}}{k}\right)\right] \tag{49}$$

where μ is related to the surface attachment kinetics and the constant $A \approx 5/6$. Kinetic effects can be ignored by setting $\mu = \infty$, which reduces Eq. (49) to Eq. (15) [16].

References

[1] C.M. Allison, G.A. Berna, L.J. Siefken, Draft preliminary report for comment: SCDAP/MOD1 theory and models, Idaho National Engineering Laboratory Informal Report, 1985.
[2] W.J. Camp, M.F. Young, J.L. Tomkins, J.E. Kelly, P.J. Maudlin, R.J. Henninger, MELPROG-PWR/MODO: A Mechanistic Code for Analysis of Reactor Core Melt Progression and Vessel Attack Under Severe Accident Conditions, NUREG/CR-4909 SAND85-0237 R3, Sandia National Laboratories, April 1987.
[3] H.E. Sills, ELOCA Fuel Element Behaviour During High-Temperature Transients, Atomic Energy of Canada Limited Report, AECL-6357, March 1979.
[4] M.S. Veshchunov, R. Dubourg, V.D. Ozrin, V.E. Shestak, V.I. Tarasov, R. Dubourg, G. Nicaise, Nucl. Eng. Des. 236 (2006) 179.
[5] M.S. Veshchunov, V.D. Ozrin, V.E. Shestak, V.I. Tarasov, J. Nucl. Mater. (2007), doi:10.1016/jnucmat2007.01.081.
[6] J.D. Higgs, B.J. Lewis, W.T. Thompson, Z. He, J. Nucl. Mater. 366 (2007) 99.
[7] B.J. Lewis, W.T. Thompson, F. Akbari, D.M. Thompson, C. Thurgood, J. Higgs, J. Nucl. Mater. 328 (2004) 180.
[8] J.C. Ramirez, M. Stan, P. Cristea, J. Nucl. Mater. 359 (2006) 174.
[9] D. Manara, C. Ronchi, M. Sheindlin, M. Lewis, M. Brykin, J. Nucl. Mater. 342 (2005) 148.
[10] R.E. Latta, R.E. Fryxell, J. Nucl. Mater. 35 (1970) 195.
[11] V. Atrazhev, M. Brykin, Numerical simulation of melting and solidification of binary mixtures in laser heating pulses (non-congruent phase transition solid–liquid), Study Contract No. 17644-2001-03F1SC KAR RU Final Report (ITU).
[12] M. Sheindlin, D. Staicu, C. Ronchi, L. Game-Arnaud, B. Remyand, A. DeGiovanni, J. Appl. Phys. 101 (2007).
[13] J. Crank, Free and Moving Boundary Problems, Oxford University Press, New York, 1984.
[14] T.C. Illingworth, I.O. Golosnoy, J. Comput. Phys. 209 (2005) 207.
[15] J.C. Ramirez, C. Beckermann, A. Karma, H.-J. Diepers, Phys. Rev. E 69 (2004).
[16] W.J. Boettinger, J.A. Warren, C. Beckermann, A. Karma, Annu. Rev. Mater. Res. 32 (2002) 163.
[17] Z. Bi, R.F. Sekerka, Physica A 261 (1998) 95.
[18] S. Kou, Transport Phenomena and Materials Processing, John Wiley & Sons Inc., New York, 1996.
[19] J. Donea, H. Antonio, J.-Ph. Ponthot, A. Rodríguez-Ferran, The Encyclopedia of Computational Mechanics, Wiley, 2004. pp. 413–437.
[20] J.W. Cahn, J.E. Hilliard, J. Chem. Phys. 28 (1958) 258.
[21] U. Hecht, L. Gránásy, T. Pusztai, et al., Materials Science and Engineering R 46 (2004) 1.
[22] M.J. Welland, B.J. Lewis, W.T. Thompson, in: Proceedings of the 30th CNS/CSA Student Conference, CNS-SNC 2006.
[23] C.H.P. Lupis, Chemical Thermodynamics of Materials, Elsevier Science Publishing Co., Inc., New York, 1983.
[24] S.R. deGroot, P. Mazur, Non-equilibrium Thermodynamics, General Publishing Company, Ltd., Toronto, ON, 1984.
[25] D. Manara, Melting Transition Measurements in Uranium Dioxide, PhD thesis, University of Warwick, 2004.
[26] J. R Welty, C.E. Wicks, R.E. Wilson, Fundamentals of Momentum, Heat and Mass Transfer, 3rd Ed., John Wiley & Sons, Inc., New York, 1984.
[27] N.B. Vargaftik, Y.D. Vasilvskaya, J. Eng. Phys. 42 (1982) 296.
[28] B.J. Lewis, B.J. Corse, W.T. Thompson, M.H. Kaye, F.C. Iglesias, P. Elder, R. Dickson, Z. Liu, J. Nucl. Mater. 252 (1998) 235.
[29] M. Tetenbaum, P.D. Hunt, J. Nucl. Mater. 34 (1970) 86.
[30] J.K. Fink, J. Nucl. Mater. 279 (2000) 1.
[31] C. Ronchi, I.L. Iosilevski, E.S. Yakub, Equation of State of Uranium Dioxide: Data Collection, Springer-Verlag, Berlin, Heidelberg, 2004.
[32] O. Penrose, P.C. Fife, Physica D 43 (1990) 44.
[33] R.F. Sekerka, J. Cryst. Growth 264 (2004) 530.
[34] F.F. Huang, Engineering Thermodynamics: Fundamentals and Applications, Macmillian Publishing Co, Inc., New York, 1976.
[35] G. Arfken, H. Weber, Mathematical Methods for Physicists, 5th Ed., Academic Press, San Diego, 2001.
[36] J.W. Cahn, J.E. Hilliard, J. Chem. Phys. 31 (3) (1959) 688.
[37] L. Gránásy, T. Pusztai, T. Börzsönyi, G. Tóth, G. Tegze, J.A. Warren, J.F. Douglas, J. Mater. Res. 21 (2006) 309.
[38] D.M. Herlach, R. Willnecker, Undercooling and Solidification, in: H.H. Liebermann (Ed.), Rapidly Solidified Alloys, Marcel Dekker Inc., New York, 1993.
[39] K. Fisher, Fundamentals of Solidification, 4th Ed., Trans Tech Publishing Ltd., Uetikon-Zuerich, Switzerland, 1998.
[40] S.L. Wang, R.F. Sekerka, A.A. Wheeler, B.T. Murray, S.R. Coriell, R.J. Braun, G.B. McFadden, Physica D 69 (1993) 189.
[41] A. Karma, W.J. Rappel, Phys. Rev. E 54 (1996) R3017.